

## Investigation of radioactivity-induced backgrounds in EXO-200

J.B. Albert,<sup>1</sup> D.J. Auty,<sup>2, a</sup> P.S. Barbeau,<sup>3</sup> D. Beck,<sup>4</sup> V. Belov,<sup>5</sup> C. Benitez-Medina,<sup>6, b</sup> M. Breidenbach,<sup>7</sup> T. Brunner,<sup>8</sup> A. Burenkov,<sup>5</sup> G.F. Cao,<sup>9</sup> C. Chambers,<sup>6</sup> B. Cleveland,<sup>10, c</sup> M. Coon,<sup>4</sup> A. Craycraft,<sup>6</sup> T. Daniels,<sup>7</sup> M. Danilov,<sup>5</sup> S.J. Daugherty,<sup>1</sup> C.G. Davis,<sup>11, d</sup> J. Davis,<sup>7</sup> S. Delaquis,<sup>12</sup> A. Der Mesrobian-Kabakian,<sup>10</sup> R. DeVoe,<sup>8</sup> T. Didberidze,<sup>2</sup> A. Dolgolenko,<sup>5</sup> M.J. Dolinski,<sup>13</sup> M. Dunford,<sup>14</sup> W. Fairbank Jr.,<sup>6</sup> J. Farine,<sup>10</sup> W. Feldmeier,<sup>15</sup> P. Fierlinger,<sup>15</sup> D. Fudenberg,<sup>8</sup> G. Giroux,<sup>12, e</sup> R. Gornea,<sup>12</sup> K. Graham,<sup>14</sup> G. Gratta,<sup>8</sup> C. Hall,<sup>11</sup> S. Herrin,<sup>7</sup> M. Hughes,<sup>2</sup> M.J. Jewell,<sup>8</sup> X.S. Jiang,<sup>9</sup> A. Johnson,<sup>7</sup> T.N. Johnson,<sup>1</sup> S. Johnston,<sup>16</sup> A. Karelin,<sup>5</sup> L.J. Kaufman,<sup>1</sup> R. Killick,<sup>14</sup> T. Koffas,<sup>14</sup> S. Kravitz,<sup>8</sup> A. Kuchenkov,<sup>5</sup> K.S. Kumar,<sup>17</sup> D.S. Leonard,<sup>18</sup> C. Licciardi,<sup>14</sup> Y.H. Lin,<sup>13</sup> J. Ling,<sup>4</sup> R. MacLellan,<sup>19</sup> M.G. Marino,<sup>15, f</sup> B. Mong,<sup>10</sup> D. Moore,<sup>8</sup> R. Nelson,<sup>20</sup> A. Odian,<sup>7</sup> I. Ostrovskiy,<sup>8</sup> A. Piepke,<sup>2</sup> A. Pocar,<sup>16</sup> C.Y. Prescott,<sup>7</sup> A. Rivas,<sup>7</sup> P.C. Rowson,<sup>7</sup> J.J. Russell,<sup>7</sup> A. Schubert,<sup>8</sup> D. Sinclair,<sup>21, 14</sup> E. Smith,<sup>13</sup> V. Stekhanov,<sup>5</sup> M. Tarka,<sup>17</sup> T. Tolba,<sup>12</sup> R. Tsang,<sup>2</sup> K. Twelker,<sup>8</sup> J.-L. Vuilleumier,<sup>12</sup> A. Waite,<sup>7</sup> J. Walton,<sup>4</sup> T. Walton,<sup>6</sup> M. Weber,<sup>8</sup> L.J. Wen,<sup>9</sup> U. Wichoski,<sup>10</sup> J. Wood,<sup>20</sup> L. Yang,<sup>4</sup> Y.-R. Yen,<sup>13</sup> and O.Ya. Zeldovich<sup>5</sup>

(EXO-200 Collaboration)

<sup>1</sup>Physics Department and CEEM, Indiana University, Bloomington, Indiana 47405, USA<sup>2</sup>Department of Physics and Astronomy, University of Alabama, Tuscaloosa, Alabama 35487, USA<sup>3</sup>Department of Physics, Duke University, and Triangle Universities Nuclear Laboratory (TUNL), Durham, North Carolina 27708, USA<sup>4</sup>Physics Department, University of Illinois, Urbana-Champaign, Illinois 61801, USA<sup>5</sup>Institute for Theoretical and Experimental Physics, Moscow, Russia<sup>6</sup>Physics Department, Colorado State University, Fort Collins, Colorado 80523, USA<sup>7</sup>SLAC National Accelerator Laboratory, Stanford, California 94025, USA<sup>8</sup>Physics Department, Stanford University, Stanford, California 94305, USA<sup>9</sup>Institute of High Energy Physics, Beijing, China<sup>10</sup>Department of Physics, Laurentian University, Sudbury, Ontario P3E 2C6, Canada<sup>11</sup>Physics Department, University of Maryland, College Park, Maryland 20742, USA<sup>12</sup>LHEP, Albert Einstein Center, University of Bern, Bern, Switzerland<sup>13</sup>Department of Physics, Drexel University, Philadelphia, Pennsylvania 19104, USA<sup>14</sup>Physics Department, Carleton University, Ottawa, Ontario K1S 5B6, Canada<sup>15</sup>Technische Universität München, Physikdepartment and Excellence Cluster Universe, Garching 80805, Germany<sup>16</sup>Amherst Center for Fundamental Interactions and Physics

Department, University of Massachusetts, Amherst, MA 01003, USA

<sup>17</sup>Department of Physics and Astronomy, Stony Brook University, SUNY, Stony Brook, New York 11794, USA<sup>18</sup>IBS Center for Underground Physics, Daejeon, Korea<sup>19</sup>Physics Department, University of South Dakota, Vermillion, South Dakota 57069, USA<sup>20</sup>Waste Isolation Pilot Plant, Carlsbad, New Mexico 88220, USA<sup>21</sup>TRIUMF, Vancouver, BC, Canada

(Dated: July 17, 2015)

The search for neutrinoless double-beta decay ( $0\nu\beta\beta$ ) requires extremely low background and a good understanding of their sources and their influence on the rate in the region of parameter space relevant to the  $0\nu\beta\beta$  signal. We report on studies of various  $\beta$ - and  $\gamma$ -backgrounds in the liquid-xenon-based EXO-200  $0\nu\beta\beta$  experiment. With this work we try to better understand the location and strength of specific background sources and compare the conclusions to radioassay results taken before and during detector construction. Finally, we discuss the implications of these studies for EXO-200 as well as for the next-generation, tonne-scale nEXO detector.

## I. INTRODUCTION

Neutrinoless double-beta decay ( $0\nu\beta\beta$ ) is a hypothetical process that may be observable in even-even nuclei in which normal  $\beta$ -decay is either energetically disallowed or highly forbidden. The discovery of this lepton-number-violating decay would indicate that the neutrino is a massive Majorana particle [1]. Current best limits from  $^{136}\text{Xe}$  [2, 3] and  $^{76}\text{Ge}$  [4] require the  $0\nu\beta\beta$  half-life to be greater than  $\sim 10^{25}$  y, posing significant experimental challenges for experiments seeking to improve detector

<sup>a</sup> Present address: University of Alberta, Edmonton, AB, Canada<sup>b</sup> Present address: Intel Corporation, Hillsboro, OR, USA<sup>c</sup> Also SNOLAB, Sudbury, ON, Canada<sup>d</sup> Present address: Naval Research Lab, Washington D.C., USA<sup>e</sup> Present address: Dept. of Physics, Queen's University, Kingston, ON, Canada<sup>f</sup> Corresponding author: michael.marino@mytum.de

reach. The challenge of identifying and rejecting backgrounds at the low energies of interest necessitates the use of radio-clean detector materials, passive and active shielding, and sophisticated analysis techniques (e.g. signal pattern recognition).

The background expectation, including the predicted counts detected in the  $0\nu\beta\beta$  signal region and the event distribution arising from internal and external background sources, is essential both for the optimization of detector design prior to construction, as well as for the analysis and interpretation of data. Only a quantitative understanding of the background expectation value, based on various observables, allows the identification of a possible event excess with the existence of a  $0\nu\beta\beta$  signal. We present investigations on  $\beta$ - and  $\gamma$ -backgrounds to the EXO-200  $0\nu\beta\beta$  experiment, comparing current results with those produced prior to detector operation and discussing the implications both for the continued running of the EXO-200 detector as well as for the proposed, tonne-scale nEXO detector.

A comprehensive description of EXO-200 may be found in [5]. The detector is a cylindrical liquid xenon (LXe) time projection chamber (TPC), roughly 40 cm in diameter and 44 cm in length. The LXe is enriched to 80.6% in  $^{136}\text{Xe}$ , the  $0\nu\beta\beta$  candidate ( $Q = 2457.83 \pm 0.37$  keV [6]). Energy depositions in the xenon produce both scintillation light and charge. The scintillation light is detected by 468 avalanche photodiodes (APDs) on both ends of the TPC. The electric field produced by the negatively biased cathode at the center of the TPC sweeps the ionization electrons to the two ends, where they are collected on wire planes. Cu rings, supported by acrylic spacers, form the field cage surrounding the drift region, assuring a uniform electric field. Inside of this cage is a cylindrical Teflon<sup>®</sup> light reflector. The two wire planes at either end of the TPC are each composed of collection (U) wires and induction (V) wires crossed at 60 degrees. The signals from both U- and V-wires are read out. The APDs are situated behind the U- and V-wires, resulting in good light transmission. Behind the APD mounts on each side of the TPC are flat polyimide signal-readout cables, which are separated from the Cu bulkhead by a layer of Teflon<sup>®</sup>. A Cu tube assembly used for the deployment of calibration sources is located just outside the TPC. A more detailed view of the components in and around the TPC may be seen in Figs. 1 and 2.

The TPC is surrounded on all sides and kept at  $\sim 167$  K by  $\sim 50$  cm of HFE-7000 cryofluid [7] (HFE) that is housed inside a double-walled vacuum-insulated Cu cryostat. Six copper supports ('TPC legs') mount the TPC to the removable hatch of the cryostat and provide a conduit for additional signal cables. The HFE further acts as a shield from external radioactivity. A Pb shield of  $\sim 25$  cm thickness, located outside the Cu cryostat, provides additional shielding. This apparatus is in a cleanroom located underground at a depth of  $1585^{+11}_{-6}$  meters water equivalent [8] at the Waste Isolation Pilot Plant (WIPP) near Carlsbad, NM, USA. Four of the six sides of the clean-

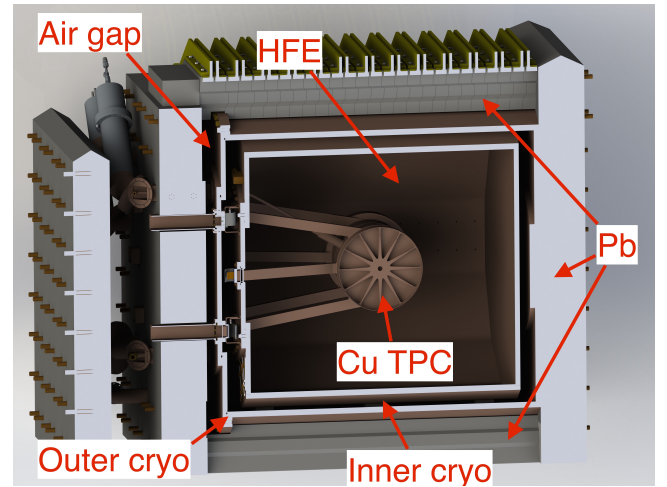


FIG. 1. (Color online) Cutaway engineering drawing of the EXO-200 detector showing the relationship between the TPC, HFE, Cu cryostats and Pb shield. The TPC, mounted on the wall of the inner cryostat with six copper supports, is surrounded by HFE cryogenic fluid. A vacuum layer lies between the inner and outer cryostats, and an air layer ('Air gap') between the outer cryostat and the Pb shield. The clean room and surrounding active muon veto detectors are omitted for clarity.

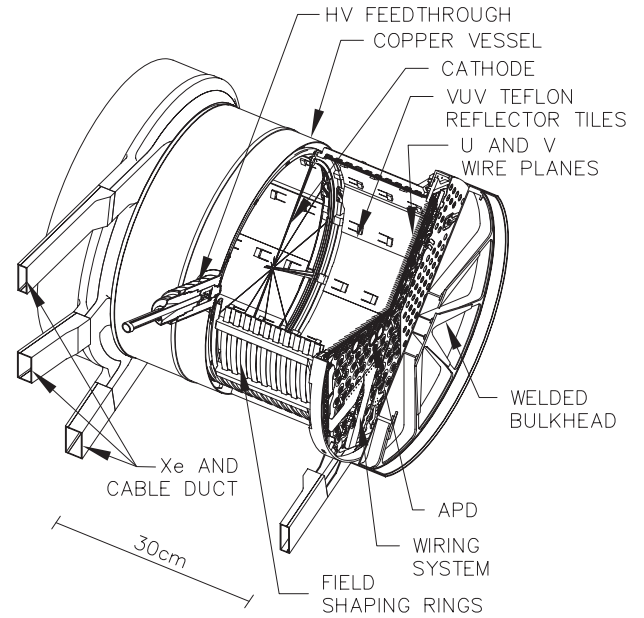


FIG. 2. Cutaway view of the EXO-200 Cu TPC. 'Wiring system' refers to the flat polyimide cables behind the APD platter. Additional flat polyimide cables are within the Cu TPC legs ('Cable duct' in figure). Acrylic spacers, insulators and field cage resistors are components of the as shown 'Field shaping rings' system, and are all external to the Teflon<sup>®</sup> reflectors ('VUV (Vacuum Ultraviolet) Teflon Reflector Tiles'). A Cu tube and support system used for deployment of calibration sources outside the Cu vessel is not shown.

room are instrumented with large plastic scintillator panels, providing  $96.0 \pm 0.5\%$  coverage of muon-associated events detected in the TPC. This efficiency is determined by measuring the percentage of muons passing through the TPC (events tagged at  $> 99.9\%$  efficiency) that also correspond to muon veto panel events.

The data analysis methods used in EXO-200 are described in [9]. Detector events are reconstructed to determine: (1) event multiplicity, (2) event position, and (3) total event energy. The ‘event multiplicity’ refers to the number of charge deposits reconstructed for a particular event; ‘single-site’ (SS) is used to refer to events with only one discernible charge deposit (with a characteristic radius of  $\sim 2\text{-}3$  mm) and ‘multi-site’ (MS) to those with two or more. This quantity allows powerful discrimination between signal and background: in the EXO-200 detector,  $0\nu\beta\beta$  events are  $\sim 90\%$  SS, whereas  $\gamma$ s with energies around the  $\beta\beta$  Q-value are 20-30% SS. The event position is determined by combining information from the APDs and U-/V-wires. The total energy of the event is measured in both the charge and light channels, which are then linearly combined to improve the energy resolution [10].

In the following sections, unless otherwise specified, we present results using ‘low-background data’, or data passing all data quality selection requirements, corresponding to  $477.60 \pm 0.01$  days of live-time accumulated in the period from September 22, 2011 to September 1, 2013 (Run 2). Limits on the  $0\nu\beta\beta$  decay of  $^{136}\text{Xe}$  using these data have been presented in Ref. [3].

To search for a  $0\nu\beta\beta$  signal in the data, a fit is performed minimizing a negative log-likelihood function constructed using a signal and background model composed of probability density functions (PDFs) from simulation. The fit proceeds over both multiplicity categories (SS and MS) and uses the observables energy and ‘standoff distance’ (SD), the latter a parameterization of the position of an event in the detector. The background model is composed of the combination of all expected background sources contributing a non-negligible number of counts to the data. The list of sources is based on information from assays of the materials used in the detector construction. These, combined with results from simulation, provide an estimate of the expected strengths of contributions from various sources and locations. In principle, this set includes a large number of different components for each separate detector piece, but in practice the shapes of the energy and SD distributions for many of these are degenerate and therefore indistinguishable in the data. For this reason, we include only the following components in our background model:

- Cu TPC vessel:  $^{40}\text{K}$ ,  $^{54}\text{Mn}$ ,  $^{60}\text{Co}$ ,  $^{65}\text{Zn}$ ,  $^{232}\text{Th}$ , and  $^{238}\text{U}$
- LXe:  $^{135}\text{Xe}$ ,  $^{137}\text{Xe}$  and  $^{222}\text{Rn}$ ,
- Air gap between Cu cryostat and Pb shield:  $^{222}\text{Rn}$
- ‘Far-source’  $^{232}\text{Th}$  (in Cu cryostat),

- neutron-capture related:  $^{136}\text{Xe}$  neutron capture in the LXe,  $^1\text{H}$  neutron-capture in the HFE, and  $^{63}\text{Cu}$ ,  $^{65}\text{Cu}$  neutron capture in Cu components (LXe vessel, inner and outer cryostats)

Note that, because of the aforementioned degeneracies, the Cu TPC vessel PDF includes contributions from background sources at a similar radius (i.e. APDs, signal cables, Cu calibration tube etc.). The inclusion of  $^{222}\text{Rn}$  in the air gap between the Cu cryostat and Pb shield accounts for a far-source of  $^{238}\text{U}$ .  $^{220}\text{Rn}$  is not included because of its short half-life and because measurements of the clean-room air indicated only negligible amounts in comparison to  $^{222}\text{Rn}$ . For construction of the PDFs, the  $^{232}\text{Th}$  and  $^{238}\text{U}$  chains are assumed to be in secular equilibrium; we find no evidence from the data that this assumption is unwarranted. The component fit degeneracy is not important for the computation of the background expectation value as different assignments would lead to the same background rate. However, our ability to unfold quantitative values for the radioactivity content of these components is limited by this.

In the following sections, we analyze the predictions from assays for  $^{232}\text{Th}$  and  $^{238}\text{U}$  and compare to measurements from data, focusing on the  $\pm 2\sigma$  energy range around the  $0\nu\beta\beta$  Q-value (ROI). Using low-background data, we investigate the placement of  $^{232}\text{Th}$  and  $^{238}\text{U}$  and look at the time behavior of different backgrounds over the Run 2 time period. We look for evidence of  $^{137}\text{Xe}$  production, and present results on the presence of  $^{222}\text{Rn}$  in the LXe and in air outside the cryostat.

## II. BACKGROUND EXPECTATIONS

We have used results from assays of  $^{232}\text{Th}$  and  $^{238}\text{U}$  in detector materials to compute the expected counts in the  $0\nu\beta\beta$  ROI, defined as the measured activity (mBq, from [5, 12]) multiplied by the efficiency calculated from the EXO-200 Geant4-based [11] Monte Carlo simulation package (MC), see e.g. [9]. Most of the assay results used in this work were at hand before construction [12], with the exception of new neutron activation results of the Teflon<sup>®</sup> used in detector construction. These new results indicated a higher total expected  $^{232}\text{Th}$  activity of  $46 \pm 4$   $\mu\text{Bq}$  (attributed to activity on the Teflon<sup>®</sup> surface) than the limits presented in Ref. [5]. Similar estimates of counts in the  $0\nu\beta\beta$  ROI were presented previously in [5] with an earlier Geant3-based [13] version of the simulation software. (The newer simulation also includes more detailed geometries and more advanced electronic signal generation.) The summary of these are shown together with the current results in Table I. In addition, we compare the total expected counts in the ROI for  $^{232}\text{Th}$  and  $^{238}\text{U}$  to the results from a maximum-likelihood fit to the low-background data [3].

Ref. [5] also included results for  $^{40}\text{K}$  due to its relevance as a background for  $2\nu\beta\beta$ , but we omit these in the presentation of Table I here because they do not contribute

TABLE I. Expected SS event rates (90% CL) in the  $\pm 2\sigma$   $0\nu\beta\beta$  ROI (with  $\sigma/E = 1.53\%$  [3]) from  $^{232}\text{Th}$  and  $^{238}\text{U}$  backgrounds from different detector components. These have been calculated using the Geant4-based [11] Monte Carlo simulation [9] of the EXO-200 detector and from assay results [12]. An exception is ‘Pb shielding’, whose results presented in this table are from Ref. [5]. See text and Figs. 1 and 2 for more details on the location of different components. For assay results producing a measurement of activity (as opposed to an upper limit), the 90% CL range of expected event rates are given. The lower (upper) limit of the total predicted rate is produced by summing the lower (upper) limits of each component. This results in a conservative bracketing of the expectation values. A summary of previous results presented in [5] and produced with an earlier Geant3-based [13] version of the EXO-200 simulation software are shown for comparison. These previous results used a slightly larger ROI ( $\sigma/E = 1.6\%$ ). The rates for backgrounds from  $^{232}\text{Th}$  and  $^{238}\text{U}$  estimated from the fit to low-background data [3] are also given for comparison.

Part/Material	Expected counts in $0\nu\beta\beta$ ROI (Cts / yr)	
	$^{232}\text{Th}$	$^{238}\text{U}$
APDs	< 0.6	< 0.05
Bronze cathode	$(6 - 10) \cdot 10^{-5}$	$(6 - 8) \cdot 10^{-3}$
Bronze wires	0.04 – 0.07	0.07 – 0.08
Other Bronze	0.08 – 0.13	0.25 – 0.3
Flat cables (in TPC)	< 0.44	1.5 – 2.3
Flat cables (in TPC Legs)	< 0.04	0.1 – 0.14
Teflon <sup>®</sup> reflectors, HV insulators	0.06 – 0.1	< 0.07
Teflon <sup>®</sup> behind APDs	0.2 – 0.3	< 0.08
Acrylic spacers, insulators	< 0.3	< 0.6
Field cage resistors	< 0.01	< 0.01
Cu TPC vessel	< 3	< 3.8
Cu TPC legs	< 0.07	< 0.05
HV cable	< 0.13	< 0.6
Cu calibration tube + support	0.1 – 0.2	0.15 – 0.35
Cu cryostat	< 1.3	< 0.5
HFE-7000	< 0.1	< 0.1
Pb shielding	< 0.9	< 0.5
Total predicted rates (sum):	0.5 – 7.7	2 – 9.5
Total predicted rates from Ref. [5]:	0.9 – 10.3	6.3 – 26.8
Observed rates from Ref. [3]:	10.3 – 13.9	5.3 – 7.1

to the  $0\nu\beta\beta$  ROI. The results of the low-background fit are however consistent with estimates of the contributions of  $^{40}\text{K}$ .

The results from the pre- and post-data-taking simulations are in good agreement, although the current numbers are somewhat lower. This can be understood as owing to a better measured resolution at the  $\beta\beta$  Q-value

( $\sigma/E = 1.53\%$  [3]) and improvements in the simulation software including more realistic geometries and a better estimation of the SS/MS discrimination. The predicted rates from assay and the observed rates of  $^{232}\text{Th}$  and  $^{238}\text{U}$  from the fit to low-background data also show reasonable agreement, although the prediction for  $^{232}\text{Th}$  backgrounds is slightly lower than that observed in the data.

Results from [3] indicate that  $^{137}\text{Xe}$  is another important background in the  $0\nu\beta\beta$  ROI. This short-lived species ( $\tau = 229.1 \pm 0.8$  s [14]) is produced by neutron capture on  $^{136}\text{Xe}$  in LXe and estimates from simulation of its production in the LXe are consistent with the experimental results. Here we present an analysis searching for evidence of the production of  $^{137}\text{Xe}$  in coincidence with cosmic-ray-muon events. More details concerning the production of  $^{137}\text{Xe}$  and the detection of the associated radiative neutron capture as well as the impact of other cosmogenic backgrounds to the search for  $0\nu\beta\beta$  with the EXO-200 detector will be published separately.

We have explored the possibility that better constraints on intrinsic activities in detector components may be produced by using the low-background data. In other words: given the observed rates, we can derive an estimate on the activities in detector components. This uses conservative assumptions, specifically that all the counts assigned to a particular PDF *type* in the low-background fit (e.g.  $^{40}\text{K}$ ,  $^{232}\text{Th}$ ,  $^{238}\text{U}$ ) are coming exclusively from one component. This approach lifts the fit component degeneracy at the expense of sensitivity. By construction it yields only limits as no fitting is performed. For almost all components, this produces weaker limits than the assay. Exceptions are  $^{40}\text{K}$  and  $^{238}\text{U}$  in the Cu TPC vessel, where the results from low-background data are more constraining than, or very similar to, those from assay. Results from low-background data yield limits on  $^{40}\text{K}$  ( $^{238}\text{U}$ ) in the Cu TPC vessel of < 1.6 mBq/kg (< 0.07 mBq/kg), which one can compare to results from assay: < 1.8 mBq/kg (< 0.05 mBq/kg). Full results from this study are presented in Table II.

### III. INVESTIGATIONS OF BACKGROUND COMPONENTS

#### A. Location of $^{232}\text{Th}/^{238}\text{U}$

Analyzing the relative strengths of peaks in the energy spectrum can yield information on the position of a particular background source. This is because the  $\gamma$  attenuation length varies versus energy and spectral features (e.g. summation peaks) depend upon the coincident detection of 2 or more separate  $\gamma$ s (see e.g. Fig. 3). We have used the latter to investigate the location of  $^{232}\text{Th}$  in detector materials by analyzing the ratio of the summation peak at 3197 keV (from 2615 and 583 keV  $\gamma$ s) to the 2615 keV  $\gamma$  peak in MS data. The ratio is constructed from the number of counts in each peak, defined by inte-

TABLE II. Upper limits (90% CL) on detector material activity (mBq) estimated using low-background data (‘This meas.’ columns)— see text for more details. See Figs. 1 and 2 for a visualization of the placement of different components. Several sets of components share similar positions in the detector construction. These produce degenerate signals in the detector and therefore have the same absolute activity limits. Assay results from Ref. [5] and neutron activation measurements of the Teflon<sup>®</sup> <sup>232</sup>Th and <sup>238</sup>U surface activity are included for comparison (‘Assay’ columns). Limits from Ref. [5] are at 90%CL. The error bars for assays producing a measurement of activity (instead of a limit) in Ref. [5] are  $\pm 1\sigma$  and have been expanded here to 90% CL. Calculations for <sup>40</sup>K for a number of small components were not performed.

Part/Material	Quantity	Detector material activity (mBq)					
		<sup>40</sup> K		<sup>232</sup> Th		<sup>238</sup> U	
		Assay	This meas.	Assay	This meas.	Assay	This meas.
APDs	518 units	< 0.13	< 31	< 0.09	< 1.0	< 0.011	< 1.7
Bronze cathode	0.010 kg	< 0.019	—	$0.00108 \pm 0.00019$	< 12	$0.00364 \pm 0.00021$	< 9.7
Bronze wires	0.083 kg	< 0.16	< 51	$0.0090 \pm 0.0015$	< 1.9	$0.0302 \pm 0.0017$	< 2.4
Other Bronze	0.314 kg	< 0.6	< 51	$0.0176 \pm 0.0027$	< 1.9	$0.107 \pm 0.006$	< 2.4
Flat cables (TPC)	7406 cm <sup>2</sup>	< 0.9	< 31	< 0.07	< 1.5	$0.43 \pm 0.06$	< 1.7
Flat cables (TPC Legs)	10825 cm <sup>2</sup>	< 1.4	< 840	< 0.07	< 23	$0.76 \pm 0.09$	< 36
Teflon <sup>®</sup> (surface)							
behind APDs, HV insulators	43400 cm <sup>2</sup>	—	—	$0.040 \pm 0.004$	< 1.5	< 0.113	< 1.66
reflectors	1660 cm <sup>2</sup>	—	—	$0.006 \pm 0.001$	< 0.73	$0.004 \pm 0.001$	< 0.84
Acrylic spacers, insulators	1.460 kg	< 0.14	—	< 0.024	< 0.73	< 0.07	< 0.84
Field cage resistors	20 units	< 0.08	—	< 0.0006	< 0.73	< 0.0017	< 0.84
Cu TPC vessel	32.736 kg	< 60	< 51	< 0.5	< 1.9	< 1.5	< 2.4
Cu TPC legs	6.944 kg	< 12	< 1000	< 0.11	< 30	< 0.33	< 50
HV cable	0.091 kg	< 5	< 95	< 0.036	< 3.0	< 0.6	< 4.2
Cu calibration tube	0.473 kg	< 8	< 126	$0.016 \pm 0.003$	< 4.8	$0.043 \pm 0.001$	< 6.5
Cu wire calibration tube support	0.144 kg	< 11	< 126	$0.027 \pm 0.002$	< 4.8	$0.19 \pm 0.06$	< 5.5
Cu cryostat	5901 kg	< 72	< $7.0 \times 10^5$	< 19	< 6500	< 58	< 18000
HFE-7000	4140 kg	< 20	< 1200	< 0.25	< 40	< 0.8	< 57

grating over the  $\pm 2\sigma$  range at their particular energies. The ratio is calculated for PDFs derived from MC for components at different locations in and around the detector, as well as for hypothetical point sources of <sup>232</sup>Th placed at varying perpendicular distances from the TPC in the same plane as the center cathode. The ratio for combined PDF components is produced by taking their normalized average, e.g.:

$$R_{\text{combined}} = \frac{\sum_i \frac{N_{3197}^i}{N_{\text{total}}^i}}{\sum_i \frac{N_{2615}^i}{N_{\text{total}}^i}} \quad (1)$$

where  $N_{3197, 2615, \text{total}}^i$  are the number of counts in the 3197 keV summation peak, in the 2615 keV peak, and in the total spectrum, respectively, for the  $i$ th PDF component. This construction assumes equal contributions from each PDF. The ratio is measured for the low-background data also by integrating in the energy regions as specified – non-<sup>232</sup>Th-related backgrounds at the relevant energies are negligible. A comparison between this number and results from MC is presented in Fig. 4. It is clear from these results that a non-negligible source of <sup>232</sup>Th background exists external to the TPC vessel. Possible locations of this source are, for example, distributed

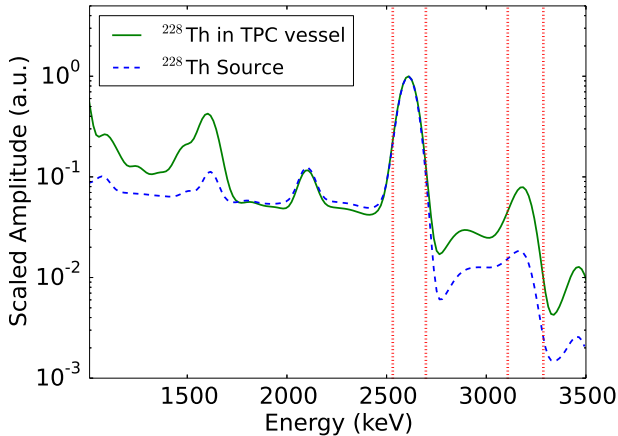


FIG. 3. (Color online) Comparison of MS PDFs for  $^{232}\text{Th}$  in the Cu TPC vessel and a  $^{228}\text{Th}$  source located just outside the TPC at the cathode. The PDFs are normalized to their respective 2615 keV peaks. The difference in spectral shapes arises from the energy-dependent attenuation length of  $\gamma$ s and because some features are created by the coincident detection of 2 or more  $\gamma$ s. The dotted (red) vertical lines indicate the energy regions over which counts are integrated to form the ratio between the 2615 keV  $\gamma$  peak and the summation peak at 3197 keV (see text).

in the surrounding HFE and/or in the Cu tube used for deployment of radioactive sources adjacent to the TPC. This is consistent with results from material assay, which indicate up to  $\sim 2.3$  counts/yr in the  $0\nu\beta\beta$  ROI may arise from  $^{232}\text{Th}$  backgrounds external to the TPC (see e.g. Table I). The uncertainty in the actual location(s) of the  $^{232}\text{Th}$  background(s) is taken into account by including the far-source  $^{232}\text{Th}$  in the background model used in the EXO-200 data analysis.

We have performed a similar study to investigate the possible presence of additional  $^{238}\text{U}$  near the detector outside the TPC vessel. The possibility of a contribution from remote  $^{238}\text{U}$  has been taken into account in the background model through the inclusion of  $^{214}\text{Bi}$  (resulting from  $^{222}\text{Rn}$  decays) in the air gap between the cryostat and Pb shield. The compatibility of this with measured Rn concentrations in the air is discussed later. In particular, we considered two additional far-source components of  $^{238}\text{U}$  (distributed in the HFE and in the external Cu cryostat) and add them, one at a time, to the background model to be fit to the low-background data. The (anti-)correlation in the fit between the one additional remote background and the already included air gap  $^{214}\text{Bi}$  was then determined. The results of the two fits indicate a strong anti-correlation between each pair of  $^{238}\text{U}$ -like PDFs. In addition, there was no statistical evidence in either of the two fits to demonstrate the presence of *both*  $^{238}\text{U}$ -like components in the data; in other words, the number of counts in one of the PDFs in each pair was always consistent with zero. Note that this does

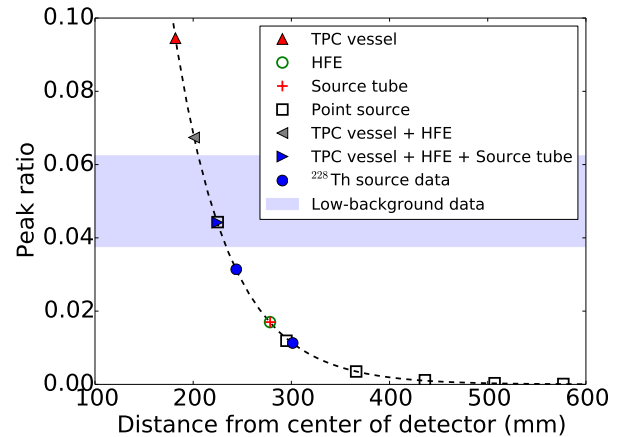


FIG. 4. (Color online) In the  $^{232}\text{Th}$  spectrum, ratios of the summation peak at 3197 keV and the 2615 keV  $\gamma$  peak for low-background and  $^{228}\text{Th}$  source data, and from simulation of  $^{232}\text{Th}$  point sources and  $^{232}\text{Th}$  distributed in particular detector components (see legend). Note, the following two pairs of points overlap: (1) ‘HFE’ and ‘Source tube’, and (2) ‘TPC vessel + HFE + Source tube’ and a ‘Point source’ at  $x \sim 220$  mm. The dashed line is an empirical fit to the simulated point sources (hollow black squares) with the form  $e^{a+bx}$ , where  $a$  and  $b$  are fitted constants. Results from source data (blue filled circles) agree well with it. The fit is used to interpolate the *effective* distance from the center of the detector for all non-point-like simulated geometries. Statistical error bars on the points are all smaller than the size of the symbols. The shaded region is from the measured value in data, where the range is due to statistical error. This region agrees best with the combination of PDFs from  $^{232}\text{Th}$  in the TPC vessel, in the Cu source tube, and distributed in the HFE, indicating the presence of a  $^{232}\text{Th}$  background source external to the TPC vessel.

not exclude the possibility of a  $^{238}\text{U}$  presence in the HFE or in the Cu cryostat, but rather indicates the degeneracy of the PDFs and the subsequent inability of the fit to distinguish between them.

## B. Time dependencies

To look for time dependencies in the data, the low-background data were divided into four time bins with roughly equal live-time. The data in each time bin were fit using the previously described procedure, and the number of counts for each PDF extracted from the fit were tracked versus time. Minor variations over time are seen in the counts for some PDFs, but these can be explained as either due to statistical fluctuations or as (anti-)correlation between PDFs of similar shape (e.g.  $^{232}\text{Th}$  in the TPC vessel and far-source  $^{232}\text{Th}$ ). We also investigated, in particular, the behavior of the  $^{60}\text{Co}$  PDF in the TPC vessel, since the total time range of data ( $\sim 710$  d) is comparable to the  $^{60}\text{Co}$  half-life ( $1925.28 \pm 0.14$  d) [17].



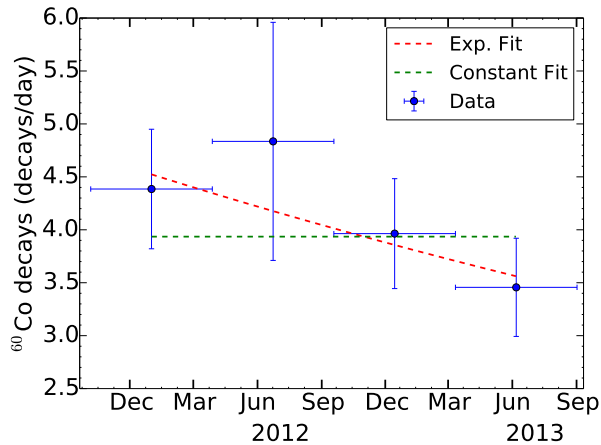


FIG. 5. (Color online) Behavior of  $^{60}\text{Co}$  fitted decay rate in the TPC vessel versus time. The rate shown is counts integrated above 980 keV. (The full range used by the fit is 980 keV–9800 keV, though the  $^{60}\text{Co}$  PDF only extends to  $\sim 2.5$  MeV). The vertical error bars on the points are those returned by the fit to the low-background data using the MIGRAD function of MINUIT [15, 16]. Horizontal error bars show the size of the time bins. Two fits to the data are shown, including a constant and an exponential fit. The exponential fit produces a half-life of  $1500 \pm 1100$  days, consistent with the half-life of  $^{60}\text{Co}$ . The  $\chi^2/\text{NDF}$  is 0.5/2 (2.35/3) for the exponential (constant) fit.

Results for this particular PDF are shown in Fig. 5. Exponential fits to these data produce values consistent with the published half-life, although with the present statistics a constant rate, such as expected for continuous production, also provides a good fit. Estimates from simulation suggest the generation of  $^{60}\text{Co}$  through cosmic-ray-muon-produced neutrons to be negligible at WIPP depth. Further detector exposure will improve the statistical power of this analysis.

### C. $^{137}\text{Xe}$

Fits to the low-background data have indicated the presence of  $^{137}\text{Xe}$  in the LXe [3], a species that  $\beta$ -decays ( $Q=4173 \pm 7$  keV) with a half-life of  $229.1 \pm 0.8$  s [14] and which may be produced by neutron capture on  $^{136}\text{Xe}$ . The ground-state decay, populated with a 67% branching ratio, produces a smooth spectrum of SS events up to its Q-value and is predominantly responsible for SS events observed above the  $^{208}\text{Tl}$  2615 keV peak. We have searched for additional evidence of  $^{137}\text{Xe}$  production following the transit of cosmic-ray muons through the TPC. Such muons (hereafter ‘TPC muons’) coincide with higher neutron flux through the TPC and therefore a higher expected neutron-capture rate on  $^{136}\text{Xe}$ . They are efficiently tagged owing to the large production of light and charge in the detector. Normally the time following

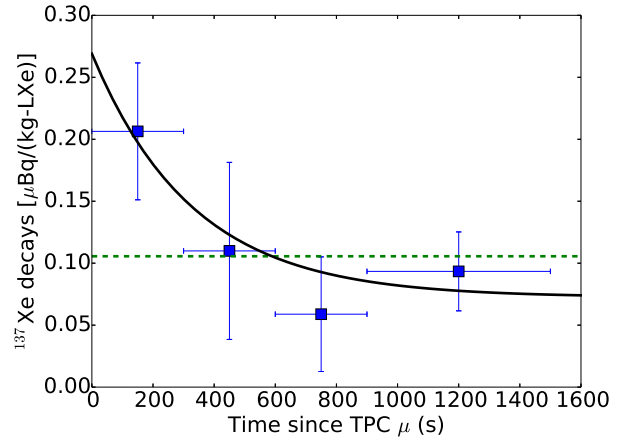


FIG. 6. (Color online)  $^{137}\text{Xe}$  decays versus time following a muon passing through the TPC. The horizontal error bars indicate the width of the time bins used. The data were fit to two functions: (1) exponential decay + constant function, with the decay fixed to the known  $^{137}\text{Xe}$  half-life, and (2) a constant. The  $\chi^2/\text{NDF}$  for 1 (2) is 0.84/2 (4.5/3), indicating a slight preference for 1.

such events is removed from the low-background data set because of the higher probability of producing short-lived radioactive species in the LXe. For this study, this selection requirement was relaxed and low-background data were binned versus time following a TPC muon. The spectral data in each time bin were fit using the standard procedure, and the behavior of the  $^{137}\text{Xe}$  PDF was tracked versus time since TPC muon. The results of this study are shown in Fig. 6. The data were fit with an exponential decay + constant function (decay constant fixed to the known  $^{137}\text{Xe}$  half-life) as well as with simply a constant. The  $\chi^2/\text{NDF}$  indicates a slight preference for the decaying function, although the results of this decay-time study are statistically still too weak to serve as direct evidence for  $^{137}\text{Xe}$  production following a TPC muon.

### D. Internal $^{222}\text{Rn}$

$^{222}\text{Rn}$  internal to the TPC (e.g. in the LXe and on the cathode) can result in background counts in the  $0\nu\beta\beta$  ROI from the decay of  $^{214}\text{Bi}$ , which has a  $\gamma$  line (2448 keV) near the  $\beta\beta$  Q-value. We continuously monitor the actual amount of  $^{222}\text{Rn}$  within the LXe by tracking counts of the 5.5 MeV decay  $\alpha$  (see Fig. 7). Energy depositions from  $\alpha$ s in the LXe are easily tagged using their distinctive charge-light ratio. In previous analyses, we find a rate of  $3.65 \pm 0.37$   $\mu\text{Bq}/(\text{kg}\cdot\text{LXe})$  corresponding to a steady-state population of  $\sim 200$   $^{222}\text{Rn}$  atoms [9]. There are three  $^{222}\text{Rn}$ -related components that may contribute background, all arising from decays of  $^{214}\text{Bi}$ : (a) in the active LXe volume, (b) on the cath-

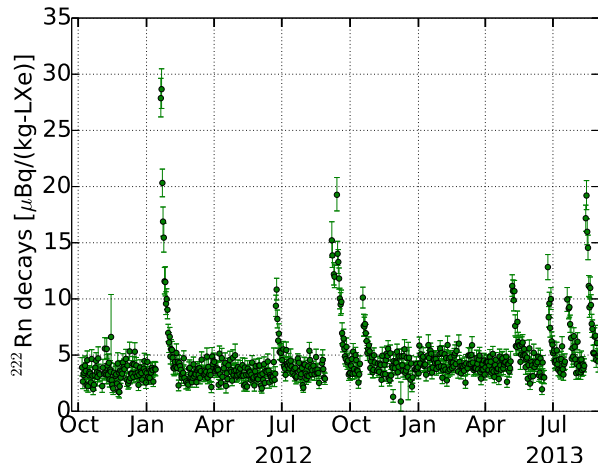


FIG. 7. (Color online)  $^{222}\text{Rn}$  decay rate in the LXe over Run 2, measured by tracking the counts of the 5.5 MeV decay  $\alpha$ . Spikes in the count rate occur when the recirculation system is upset (typically by power outages), resulting in the feed of some xenon from the bottle rack. Such xenon contains a higher amount of  $^{222}\text{Rn}$  (presumably from components in the feed plumbing system) which then decays in the detector with the expected half-life. These periods of increased  $^{222}\text{Rn}$  activity are removed from the low-background data set.

TABLE III. Background contributions (untagged) from  $^{222}\text{Rn}$  internal to the TPC vessel (inside the LXe and on the cathode) estimated using low-background data and simulation. The fiducial volume is that used in [3], corresponding to an active (inactive) LXe mass of 94.6 kg (61.7 kg). Errors on each rate are  $\pm 10\%$ .

$^{222}\text{Rn}$ component	Expected counts in $0\nu\beta\beta$ ROI (Cts / yr)
$^{222}\text{Rn}$ in the active LXe	0.011
$^{214}\text{Bi}$ on the cathode	0.14
$^{222}\text{Rn}$ in the inactive LXe	0.085
Total:	0.24

ode, and (c) in the inactive LXe volume. The decay of  $^{222}\text{Rn}$  and its daughters in the active LXe sometimes create positively-charged ions that drift towards the cathode. Only 17% of the resulting  $^{214}\text{Bi}$  decays occur in the active xenon (a), with the remaining 83% occurring on the cathode (b) [9]. A majority of the (a) and (b) decays ( $> 50\%$ ) are tagged using  $^{214}\text{Bi}$ – $^{214}\text{Po}$  decay coincidences ( $T_{1/2}^{214\text{Po}} = 163.6 \pm 0.3 \mu\text{s}$  [18]). In contrast, decays in the inactive LXe (c) are not actively tagged. We calculate the contribution of untagged events to the  $0\nu\beta\beta$  ROI using MC and present the results in Table III. The contribution of internal-Rn-related backgrounds to the  $0\nu\beta\beta$  ROI is insignificant in comparison to those from e.g. external  $^{232}\text{Th}$  and  $^{238}\text{U}$  sources.

The measurement of a constant rate of  $^{222}\text{Rn}$  decay (except for the spikes discussed in the Fig. 7 caption) in-

dicates that its population is supported, likely from the emanation from materials in contact with the LXe. This may occur either outside or inside the TPC, as the LXe is continuously circulated and purified during normal detector operation. Measurements of Rn emanation from the external xenon piping show that contributions from this system may explain the steady-state population of Rn in the LXe. For components internal to the TPC, out-gassing estimates based on the measured U content (or lack thereof) indicate that only the internal polyimide readout cables (with a surface area of  $37600 \text{ cm}^2$  in contact with LXe) could provide a significant contribution to the Rn population. Rn emanation measurements of these cables only provide upper limits on this contribution, demonstrating they are capable of supporting up to 270  $^{222}\text{Rn}$  atoms in the LXe.

### E. External $^{222}\text{Rn}$

An earlier search for  $0\nu\beta\beta$  using a smaller data set (e.g. [19]) showed an indication for an background source of  $^{238}\text{U}$  outside of the TPC vessel, possibly from  $^{222}\text{Rn}$  in the air gap between the Cu cryostat and the inside of the Pb shield. The  $^{222}\text{Rn}$  content in the cleanroom air was monitored during most of the Run 2 data-taking period using a commercial Rad7 device [20]. Pressure measurements in the air gap indicate a complete exchange with the cleanroom air every 6 minutes, implying that the  $^{222}\text{Rn}$  content of both air volumes should be in equilibrium. Measurements with the Rad7 device produce an average  $^{222}\text{Rn}$  decay rate per unit volume of  $6.6 \pm 0.3 \text{ Bq/m}^3$  over the Run 2 time period. In addition, diurnal and annual modulations in the  $^{222}\text{Rn}$  decay rate were observed, both exhibiting peak-to-peak variations of  $\sim 4 \text{ Bq/m}^3$ .

We analyze low-background data from a subset of Run 2 (ending in June 2013) and perform a fit to this data, using the standard procedure described in Section I. Using the efficiency calculated from MC, the volume in the air gap, and assuming that the far  $^{238}\text{U}$  is arising entirely from  $^{222}\text{Rn}$  in the air gap, we obtain the estimated activity of  $^{222}\text{Rn}$  in this space:  $89_{-27}^{+18} \text{ Bq/m}^3$ . This value is inconsistent with the Rad7 measurements, strongly suggesting that far-source  $^{238}\text{U}$ -like contributions are not predominantly from  $^{222}\text{Rn}$  in the air gap, but rather from other sources including the HFE or the Cu cryostat. Such contributions are still allowed by limits from material assays, which estimate a contribution from external  $^{238}\text{U}$  backgrounds in the  $0\nu\beta\beta$  ROI of up to  $\sim 1.5$  counts/yr. Additional analyses have searched for annual and diurnal modulations of this background component, by (1) binning versus time, and (2) binning the data according to time of day and fitting the spectral data of each bin. Neither search finds a statistically significant modulation.



#### IV. CONCLUSIONS

The results presented here give confidence in the background model used in previous publications with data from the EXO-200 detector. Whereas some information may be obtained from the low-background data concerning the location of background sources, it is difficult to determine exact positions because of the overall low background count rate. The EXO-200 detector and related facilities at WIPP are currently undergoing preparations for re-commissioning in 2015, following an extended data-taking hiatus owing to the closure of the WIPP underground beginning early 2014. The planned deployment of a charcoal-based Rn-suppression system should help reduce the  $^{222}\text{Rn}$  content in the air gap inside the Pb shield by a factor of 10 – 100, though current results suggest that this may not have a significant impact on the observed background. At the minimum, this will reduce  $^{222}\text{Rn}$  to such a level so as to allow one degenerate fit component to be removed from the background model. Development of analysis techniques to reduce  $^{137}\text{Xe}$  backgrounds in the data are being explored, with the goal to apply them to future and existing data sets from the EXO-200 detector.

The agreement observed between background estimates from material assay and results from fits of the EXO-200 data provides a basis for employing similar cal-

culations for the nEXO detector, a proposed 5000 kg next-generation  $0\nu\beta\beta$  experiment using LXe and based on the EXO-200 design. The analyses and comparisons presented in this paper show that careful component radio assay is able to produce both robust estimations of experiment sensitivity as well as provide guidance and constraint for its design. In addition, cosmogenic backgrounds for the nEXO detector, including  $^{137}\text{Xe}$ , will be significantly reduced by deploying to a deeper location where the cosmic-ray muon flux is at least two orders of magnitude lower than at WIPP. Estimates using simulation for  $^{137}\text{Xe}$  production at deep sites ( $> 6$  km water equivalent) indicate a reduction of at least three orders of magnitude with comparison to the WIPP site.

#### ACKNOWLEDGMENTS

EXO-200 is supported by DOE and NSF in the United States, NSERC in Canada, SNF in Switzerland, IBS in Korea, RFBR (14-02-00675) in Russia, CAS-IHEP Fund in China, and DFG Cluster of Excellence “Universe” in Germany. EXO-200 data analysis and simulation uses resources of the National Energy Research Scientific Computing Center (NERSC), which is supported by the Office of Science of the U.S. Department of Energy under Contract No. DE-AC02-05CH11231. The collaboration gratefully acknowledges the WIPP for their hospitality.

- 
- [1] J. Schechter and J.W.F. Valle, “Neutrinoless double- $\beta$  decay in  $\text{SU}(2) \times \text{U}(1)$  theories,” *Phys. Rev. D*, **25**, 2951–2954 (1982).
  - [2] A. Gando *et al.* (KamLAND-Zen Collaboration), “Limit on neutrinoless  $\beta\beta$  decay of  $^{136}\text{Xe}$  from the first phase of KamLAND-Zen and comparison with the positive claim in  $^{76}\text{Ge}$ ,” *Phys. Rev. Lett.*, **110**, 062502 (2013).
  - [3] J. Albert *et al.* (EXO-200 Collaboration), “Search for Majorana neutrinos with the first two years of EXO-200 data,” *Nature*, **510**, 229–234 (2014).
  - [4] M. Agostini *et al.* (GERDA Collaboration), “Results on neutrinoless double- $\beta$  decay of  $^{76}\text{Ge}$  from Phase I of the GERDA experiment,” *Phys. Rev. Lett.*, **111**, 122503 (2013).
  - [5] M. Auger *et al.*, “The EXO-200 detector, part I: Detector design and construction,” *JINST*, **7**, P05010 (2012).
  - [6] Matthew Redshaw, Elizabeth Wingfield, Joseph McDaniel, and Edmund G. Myers, “Mass and double-beta-decay Q value of  $^{136}\text{Xe}$ ,” *Phys. Rev. Lett.*, **98**, 053003 (2007).
  - [7] 3M™ Novec™ HFE-7000, <http://www.3m.com>, (2014).
  - [8] Ernst-Ingo Esch *et al.*, “The cosmic ray muon flux at WIPP,” *Nucl. Inst. & Meth. A*, **538**, 516–525 (2005).
  - [9] J. B. Albert *et al.* (EXO-200 Collaboration), “An improved measurement of the  $2\nu\beta\beta$  half-life of  $^{136}\text{Xe}$  with EXO-200,” *Phys. Rev. C*, **89**, 015502 (2014).
  - [10] E. Conti, R. DeVoe, G. Gratta, T. Koffas, S. Waldman, *et al.*, “Correlated fluctuations between luminescence and ionization in liquid xenon,” *Phys. Rev. B*, **68**, 054201 (2003).
  - [11] J. Allison *et al.*, “Geant4 developments and applications,” *IEEE Trans. Nucl. Sci.*, **53**, 270–278 (2006), ISSN 0018-9499.
  - [12] D.S. Leonard *et al.*, “Systematic study of trace radioactive impurities in candidate construction materials for EXO-200,” *Nucl. Inst. & Meth. A*, **591**, 490 – 509 (2008), ISSN 0168-9002.
  - [13] Computing Application Software Group and Networks Division, *GEANT – Detector Description and Simulation Tool*, Tech. Rep. CERN-W5013 (CERN, 1993).
  - [14] E. Browne and J.K. Tuli, “Nuclear data sheets for A = 137,” *Nucl. Data Sheets*, **108**, 2173 – 2318 (2007).
  - [15] R. Brun and F. Rademakers, “ROOT: An object oriented data analysis framework,” *Nucl. Inst. & Meth. A*, **389**, 81–86 (1997).
  - [16] F. James and M. Roos, “‘MINUIT’ a system for function minimization and analysis of the parameter errors and correlations,” *Comp. Phys. Comm.*, **10**, 343–367 (1975).
  - [17] E. Browne and J.K. Tuli, “Nuclear data sheets for a = 60,” *Nucl. Data Sheets*, **114**, 1849 – 2022 (2013), ISSN 0090-3752.
  - [18] M. Shamsuzzoha Basunia, “Nuclear data sheets for a = 210,” *Nucl. Data Sheets*, **121**, 561 – 694 (2014), ISSN 0090-3752.
  - [19] M. Auger *et al.* (EXO-200 Collaboration), “Search for neutrinoless double-beta decay in  $^{136}\text{Xe}$  with EXO-200,” *Phys. Rev. Lett.*, **109**, 032505 (2012).
  - [20] DURRIDGE, Rad7 Electronic Radon Detector,

<http://www.durridge.com>.